

# Limits on variations in fundamental constants from 21-cm and ultraviolet quasar absorption lines

P. Tzanavaris,<sup>1,\*</sup> J. K. Webb,<sup>1</sup> M. T. Murphy,<sup>2</sup> V. V. Flambaum,<sup>1</sup> and S. J. Curran<sup>1</sup>

<sup>1</sup>*School of Physics, The University of New South Wales,  
Sydney, NSW 2052, Australia*

<sup>2</sup>*Institute of Astronomy, Madingley Road, Cambridge CB3 0HA, United Kingdom*

(Dated: November 18, 2018)

Quasar absorption spectra at 21-cm and UV rest-wavelengths are used to estimate the time variation of  $x \equiv \alpha^2 g_p \mu$ , where  $\alpha$  is the fine structure constant,  $g_p$  the proton  $g$  factor, and  $m_e/m_p \equiv \mu$  the electron/proton mass ratio. Over a redshift range  $0.24 \lesssim z_{\text{abs}} \lesssim 2.04$ ,  $\langle \Delta x/x \rangle_{\text{total}}^{\text{weighted}} = (1.17 \pm 1.01) \times 10^{-5}$ . A linear fit gives  $\dot{x}/x = (-1.43 \pm 1.27) \times 10^{-15} \text{yr}^{-1}$ . Two previous results on varying  $\alpha$  yield the strong limits  $\Delta\mu/\mu = (2.31 \pm 1.03) \times 10^{-5}$  and  $\Delta\mu/\mu = (1.29 \pm 1.01) \times 10^{-5}$ . Our sample,  $8\times$  larger than any previous, provides the first direct estimate of the intrinsic 21-cm and UV velocity differences  $\sim 6 \text{ km s}^{-1}$ .

PACS numbers: 98.80.Es, 06.20.Jr, 95.30.Dr, 95.30.Sf

The existence of extra spatial dimensions, often invoked by superunification theories, may be inferred by the detection of spatial or temporal variations in the values of coupling constants (See [1] for a review). Spectroscopy of gas clouds which intersect the lines of sight to distant quasars is a unique tool, probing the values of these constants over a large fraction of the age of the universe. The highly sensitive many-multiplet method, developed by [2, 3], has been applied to rest-frame ultraviolet (UV) atomic quasar absorption lines to provide constraints on the possible variation of the fine structure constant,  $\alpha \equiv e^2/(\hbar c)$  [3, 4, 5, 6, 7]. Molecular hydrogen absorption lines have provided constraints on the variability of the electron-to-proton mass ratio,  $\mu$  [8, 9, 10, 11, 12].

*Principle.*— The above results have been obtained by use either of heavy element transitions, which absorb in the rest-frame UV, or of molecular hydrogen transitions. Another approach is to use the parameter  $x \equiv \alpha^2 g_p m_e/m_p$  when, as well as rest-frame UV, rest-frame 21-cm absorption, due to cold neutral hydrogen, is also detected. Rest-frame UV absorption is observed redshifted in the optical region, and rest-frame 21-cm is observed redshifted at longer radio wavelengths. The ratio of frequencies  $\omega_{21}/\omega_{\text{UV}} \propto x$ . 21-cm absorption occurs in a few damped Lyman- $\alpha$  (DLA) systems which also show heavy-element absorption in the UV. A detailed list can be found in [13]. If both UV and 21-cm absorption occur at the same physical location, the relative change of the value of  $x$  between redshifts  $z$  and 0 is related to the observed absorption redshifts for rest-frame 21-cm and UV,  $z_{21}$  and  $z_{\text{UV}}$ , according to  $\Delta x/x \equiv \frac{x_z - x_0}{x_0} = \frac{z_{\text{UV}} - z_{21}}{1 + z_{21}}$  [14]. We obtained values for  $z_{\text{UV}}$  and  $z_{21}$  by using the strongest absorption components in an absorption system. This approach is discussed in detail later.

However, as there are only 17 DLAs where both 21-cm and UV absorption have been detected, there are few results based on this method [14, 15, 16, 17]. Out

of these, only [16] use high-resolution optical data from the Keck telescope's HIRES spectrograph, but they provide an estimate of  $\Delta x/x$  at a single redshift from a single absorption system. We applied this method to eight absorption systems in eight quasar spectra (one system per spectrum), covering the absorption redshift range  $\sim 0.24$  to  $\sim 2.04$ . We used all available 21-cm absorption data in conjunction with the highest-resolution UV data available. Thus the results presented here are based on the largest dataset of the highest quality to which this method has been applied to date.

*Data analysis.*— Details of the 21-cm and UV data used are given in Table I. All redshifts are in the heliocentric frame. For the strongest component in each 21-cm absorption complex, the dispersion coordinate at the pixel of minimum intensity, MHz or  $\text{km s}^{-1}$ , was measured, from which  $z_{21}$  was obtained. We searched the optical data for heavy element absorption features close to the redshifts where there is 21-cm absorption. A number of UV absorption features were thus identified, some due to neutral species and most due to singly ionized species. For all UV spectra we determined the value of the dispersion coordinate,  $\text{\AA}$  or  $\text{km s}^{-1}$ , for the strongest component at the pixel of minimum intensity. We then determined absorption redshifts for each detected neutral or singly ionized absorption species that was not saturated. A  $z_{\text{UV}}$  value was determined individually for each transition of a single species, e.g. independently for Zn II 2026.14 and Zn II 2062.66. In all, there were 30 distinct UV species identifications (see Table I, column 6). Detailed velocity plots showing all 21-cm and UV absorption components used can be found in [18] and [19].

*Estimating  $\Delta x/x$ .*— For each absorption system we calculated  $\langle z_{\text{UV}} \rangle$ , the average of all UV absorption redshifts for single species (column 5 in Table I). Using this and our measured  $z_{21}$  (column 3 in Table I) we applied the relation between  $\Delta x/x$ ,  $z_{\text{UV}}$  and  $z_{21}$  to obtain  $\langle \Delta x/x \rangle_{\text{abs}}$ . This is the average value for  $\Delta x/x$  for each

TABLE I: Data used in this work. There is one 21-cm/UV absorption system in each quasar spectrum. Column 1 is the quasar name and Column 2 its emission redshift. Column 3 gives the 21-cm absorption redshift (and error from Column 4 references) for the strongest component. We determined this after digitizing 21-cm absorption plots (references in column 4). For Q0458–0203 the original data were used with the error taken from [20]. Column 5 gives the mean absorption redshift (and standard deviation on the observed mean) for the strongest UV component. Column 6 gives the UV heavy element species observed in the optical (with number of transitions in parentheses, if more than one). Column 7 gives the source for the UV data. Data for eight quasars were obtained from the European Southern Observatory’s (ESO) archive and were originally observed with the UVES spectrograph on the Very Large Telescope (VLT), in which case the ESO program ID is given in column 7 and the principal investigators of the program are given in footnotes. For Q1331+170 we also used Si II 1808.01Å Keck/HIRES data provided by A. Wolfe. For quasar Q0235+164 we digitized an absorption plot from the literature for a single heavy element species.

Quasar	$z_{\text{em}}$	$z_{21}$	21-cm data	$\langle z_{\text{UV}} \rangle$	ions	UV data
Q0952+179	1.478	0.237803(20)	[21]	0.237818(6)	Mg I, Ca II(2)	69.A-0371(A) <sup>a</sup>
Q1127–145	1.187	0.312656(50)	[22]	0.312648(6)	Ca II(2), Mn II(3)	67.A-0567(A) <sup>b</sup> , 69.A-0371(A) <sup>a</sup>
Q1229–021	1.038	0.394971(4)	[23]	0.395019(40)	Ca II(2), Mn II(3), Ti II	68.A-0170(A) <sup>c</sup>
Q0235+164	0.940	0.523874(100)	[24]	0.523829(6)	Mg I	[25]
Q0827+243	0.941	0.524757(50)	[21]	0.524761(6)	Ca II(2), Fe II	68.A-0170(A) <sup>c</sup> , 69.A-0371(A) <sup>a</sup>
Q1331+170	2.097	1.776427(20)	[26]	1.776355(5)	Mg I, Al II, Si II, S II, Cr I(3), Cr I*, Cr II(2), Mn II(2), Fe II(4), Ni II(6), Zn II Si II <sup>e</sup>	67.A-0022(A) <sup>d</sup> , 68.A-0170(A) <sup>c</sup> [26]
Q1157+014	1.986	1.943641(10)	[17]	1.943738(3)	Mg I, Mg II(2), Si II, Ni II(6)	65.O-0063(B) <sup>f</sup> , 67.A-0078(A) <sup>f</sup> , 68.A-0461(A) <sup>g</sup>
Q0458–0203	2.286	2.039395(80)	[26]	2.039553(4)	Zn II(2), Ni II(6), Mn II(3), Cr II(3)	66.A-0624(A) <sup>f</sup> , 68.A-0600(A) <sup>f</sup> , 072.A-0346(A) <sup>f</sup> , 074.B-0358(A) <sup>h</sup>

<sup>a</sup>Savaglio

<sup>b</sup>Lane

<sup>c</sup>Mallén-Ornelas

<sup>d</sup>D’Odorico

<sup>e</sup>Same transition as in the UVES data but from Keck/HIRES.

<sup>f</sup>Ledoux

<sup>g</sup>Kanekar

<sup>h</sup>Dessauges-Zavadsky

absorption system. We plot these results in Fig. 1.

Taking the average of all  $\langle \Delta x/x \rangle_{\text{abs}}$  values, we obtained  $\langle \Delta x/x \rangle_{\text{total}} = (0.91 \pm 1.04) \times 10^{-5}$  (‘result 1’) over an absorption redshift range  $0.24 \lesssim z_{\text{abs}} \lesssim 2.04$  and a fractional lookback time range  $0.20 \lesssim t_{\text{fb}} \lesssim 0.76$ , where we have used a Hubble parameter  $H_0 = 73 \text{ km s}^{-1} \text{ Mpc}^{-1}$ , a total matter density  $\Omega_M = 0.27$  and a cosmological constant  $\Omega_\Lambda = 0.73$ . The error quoted is the standard deviation on the mean.

We also performed the above calculations by taking into account statistical errors on  $z_{21}$  and  $\langle z_{\text{UV}} \rangle$  per absorption system (Table I). For  $z_{21}$  we used errors from the Table I references [32]. For  $\langle z_{\text{UV}} \rangle$  we used the standard deviation on  $\langle z_{\text{UV}} \rangle$  for each absorption system [33]. We obtained  $\langle \Delta x/x \rangle_{\text{total}}^{\text{weighted}} = (2.18 \pm 0.97) \times 10^{-5}$  (‘result 2’). This has a  $\chi^2$  per degree of freedom,  $\nu$ ,  $\chi^2/\nu = 8$ . We thus increased the individual errors on  $\langle \Delta x/x \rangle_{\text{abs}}$  by an additional error,  $s$ , to  $(\sigma_{\langle \Delta x/x \rangle_{\text{abs}}}^2 + s^2)^{0.5}$  until, at  $s = 1.90 \times 10^{-5}$ ,  $\chi^2/\nu = 1$ . This corresponds to  $\langle \Delta x/x \rangle_{\text{total}}^{\text{weighted}} = (1.17 \pm 1.01) \times 10^{-5}$  (‘result 3’).

For all  $\langle z_{\text{UV}} \rangle$  values per quasar absorber we calculated the average fractional lookback time per absorber,  $\langle t_{\text{fb}} \rangle_{\text{abs}}$ . We then performed an iterative linear least

squares fit to  $\langle \Delta x/x \rangle_{\text{abs}} = A \langle t_{\text{fb}} \rangle_{\text{abs}}$ , where the additional error,  $s$ , was determined at each iteration to force  $\chi^2/\nu = 1$  around the fit, obtaining  $A = (1.90 \pm 1.69) \times 10^{-5}$  [34]. It follows that the best fit rate of change of  $x$  as a function of time  $\frac{d}{dt}(\Delta x/x) = \dot{x}/x_0 = (-1.43 \pm 1.27) \times 10^{-15} \text{ yr}^{-1}$ .

*Assumptions.*— In this work we are making two assumptions. The validity of our result does not depend on the validity of these assumptions. On the contrary, we are essentially using our result to test these assumptions. Moreover, if these assumptions are incorrect, they only contribute to any observed scatter in  $\langle \Delta x/x \rangle_{\text{abs}}$ . Therefore, this possibility has already been taken into account in results 1 and 3.

1. *Strongest components:* Both the 21-cm and UV profiles exhibit complex velocity structure, i.e. have multiple absorption components at slightly different redshifts. That being the case, how does one compare the redshifts among different transitions? For neutral and singly ionized UV species, velocity structure is essentially the same and corresponding components can easily be identified. This is not the case if one compares 21-cm and UV velocity structure, although we have not systematically

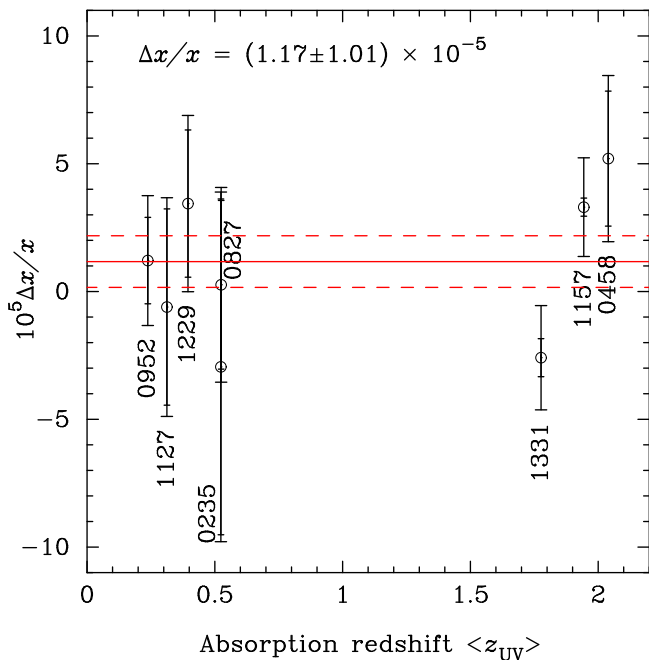


FIG. 1:  $\Delta x/x$  results for the eight absorption systems in our quasar sample. Initial (increased) error bars have shorter (longer) terminators. Quasar names are given truncated to four digits. Each point represents  $\langle \Delta x/x \rangle_{\text{abs}}$  obtained from  $z_{21}$  and  $\langle z_{UV} \rangle$ , for all heavy element species in a quasar spectrum, versus average  $\langle z_{UV} \rangle$  for that spectrum. The solid horizontal line is result 3. The dashed lines show the  $\pm 1\sigma$  range.

searched for corresponding velocity patterns in the 21-cm and UV profiles. One simple option is to measure mean absorption centroids over all components for each absorption system, which was essentially the approach taken by [16]. Alternatively one can simply determine  $z_{21}$  for the strongest component in the 21-cm profile and  $z_{UV}$  for the strongest component in each of the UV transitions, and use these. In our sample this is the only well defined quantity for both the 21-cm and the UV profiles. Additionally, this procedure, unlike mean centroiding, should have the advantage of being less sensitive to measurement errors caused by broad velocity structure in absorption lines.

*2. Neutral and singly ionized species:* We have used both neutral and singly ionized species. One might expect only the UV *neutral* gases to be spatially coincident with the 21-cm absorbing gas (unless the 21-cm gas is primordial or has very low heavy element abundances). However, it was clear in our sample that velocity structure of neutral UV species was followed closely by singly ionized species as well. This suggests that ionization fraction and abundance may not change significantly along a complex. As shown by [27], this is a general observation for DLAs. Further, the strongest component in singly ionized species corresponded well to the strongest component in neutral species. These observations justify

using singly ionized species as well. As neutral species are very rare, one obtains the substantial advantage of a much larger sample. This allowed us to investigate systematics for individual absorbers for the first time (see below).

*Errors.*— The redshift errors introduced in digitizing the data are  $< 4 \times 10^{-6}$ , (typically  $\sim 10^{-6}$ ), which is about an order of magnitude smaller than the observed intrinsic scatter on  $\Delta x/x$ . Further, for result 1, the error quoted is a standard deviation on the mean, directly reflecting the scatter in  $\langle \Delta x/x \rangle_{\text{abs}}$ . The error in result 2 was obtained after introducing errors for  $z_{21}$  and  $\langle z_{UV} \rangle$  (Table I). Although, formally, this gives a smaller error, when the errors in  $\langle \Delta x/x \rangle_{\text{abs}}$  are increased so that  $\chi^2/\nu = 1$ , results 1 and 3 for  $\langle \Delta x/x \rangle_{\text{total}}^{\text{weighted}}$  and its error are very close. This shows that *the scatter in  $\langle \Delta x/x \rangle_{\text{abs}}$  dominates any errors in individual redshift measurements*. For a single absorption complex this is a systematic error. However, for many complexes this error has random sign and magnitude. This error can be accounted for directly if treated as a statistical error when calculating the mean value of  $x$  for many absorption complexes, as we do for results 1 and 3.

*Discussion of results.*— In Fig. 1 there is considerable scatter in the values for  $\langle \Delta x/x \rangle_{\text{abs}}$ . For all spectra all optically observed species tend to group together in their  $\Delta x/x$  values on one side of zero. This is because there is significant offset between the single  $z_{21}$  value and all  $z_{UV}$  values in a system. This suggests that there *is* spatial offset between the 21-cm and UV absorbing gases, but, as expected, this is *random* for different absorbers. The error of result 1 directly reflects this scatter. A straightforward statistical calculation misses this effect (small error in result 2). Result 3 is consistent with result 1 and the value of  $s$  provides an estimate of the line of sight velocity difference  $\Delta v_{\text{los}} \sim cs = 6 \text{ km s}^{-1}$ .

One possible physical explanation for the observed offset may be a large angular size for the emitting 21-cm quasar source, as seen by the absorber. A 21-cm sightline can then intersect a cold, neutral hydrogen cloud with little or no heavy elements, whilst a UV/optical sightline can intersect another cloud with heavy elements at quite a different velocity. A large angular size is due to the combined effects of proximity of the absorber to the quasar (small  $z_{\text{em}} - \langle z \rangle$ ) and intrinsic size of the radio emitting region. Note also the good agreement with the velocity difference ( $\sim 10 \text{ km s}^{-1}$ ) between 21-cm and mm absorption lines likely due to small scale motion of the interstellar medium [28].

*Comparison with previous results.*— [16] used neutral carbon C I, C I\*, lines in the Keck/HIRES absorption spectrum of Q1331+170, to obtain  $\Delta x/x = (0.70 \pm 0.55) \times 10^{-5}$ . For the same object we obtain  $\Delta x/x = (-2.59 \pm 0.74_{\text{stat}} \pm 1.90_{\text{sys}}) \times 10^{-5}$ . The central value in [16] differs from ours because these authors used a  $z_{UV}$  value which is a weighted mean for the observed compo-

nents [29], thus obtaining a value very close to  $z_{21}$  for this absorption system. In our VLT/UVES spectrum of Q1331+170, we detected 23 distinct UV heavy element transitions whose strongest component was well defined within a few  $\text{km s}^{-1}$ . Further, our use of eight objects allows us to quantify the systematics due to the sightline issues explained above. The error in [16] is exclusively statistical, as it is based on a single absorption system. Although at face value this error is lower than ours, it inevitably contains no information on systematics, which, as our error estimate shows, dominate.

*Robustness.*— We stress that a non-zero  $\Delta x/x$  value is not corroborated by the sample as a whole, for which the result is robust. For our quoted result we have not used  $z_{\text{UV}}$  obtained from Ca II whose ionization potentials are least similar to those for all other elements used. Even so, the result changes by about 4% if Ca II is included. If we use  $z_{21}$  from the literature, rather than values determined from our digitized plots, we obtain  $\langle \Delta x/x \rangle_{\text{total}}^{\text{weighted}} = (1.51 \pm 1.04) \times 10^{-5}$  [35]. If, additionally, we do not use results for Q0235+164 or Q1127–145, thus excluding any results based on digitized plots, we obtain  $\langle \Delta x/x \rangle_{\text{total}}^{\text{weighted}} = (1.77 \pm 1.12) \times 10^{-5}$ . In all cases  $\Delta v_{\text{los}}$  remains at  $6 \text{ km s}^{-1}$  [36].

*Variation of  $\mu$ .*— Measurements of  $x \equiv \alpha^2 g_p m_e / m_p$  are sensitive to variation of several fundamental constants. The proton mass  $m_p$  is proportional to the quantum chromodynamic (QCD) scale  $\Lambda_{\text{QCD}}$ . The dependence of the proton mass on the quark mass  $m_q$  is very weak ( $\Delta m_p / m_p \approx 0.05 \Delta m_q / m_q$  [30]) and may be neglected. The dependence of the proton magnetic  $g_p$  factor on the fundamental constants is also quite weak:  $\Delta g_p / g_p \approx -0.1 \frac{\Delta(m_q / \Lambda_{\text{QCD}})}{(m_q / \Lambda_{\text{QCD}})}$  [30]. Therefore, the most important effects are due to the variations of  $\alpha$  and  $\mu \equiv m_e / m_p \approx 0.2 m_e / \Lambda_{\text{QCD}}$ . From the definition of  $x$  one obtains  $\frac{\mu_z - \mu_0}{\mu_0} \equiv \Delta \mu / \mu = \Delta x / x - 2 \Delta \alpha / \alpha - \Delta g_p / g_p$ . Using the  $\Delta \alpha / \alpha$  results of [5] and [6], we obtain  $\Delta \mu / \mu = (2.31 \pm 1.03) \times 10^{-5}$  and  $\Delta \mu / \mu = (1.29 \pm 1.01) \times 10^{-5}$ , respectively, assuming  $\Delta g_p / g_p \sim 0$ . Our result contradicts  $\Delta \mu / \mu = (-2.97 \pm 0.74) \times 10^{-5}$  [31][37] but is consistent with  $\Delta \mu / \mu = (0.5 \pm 3.6) \times 10^{-5}$ , ( $2\sigma$ ) [12]. Note that our result on  $\Delta \mu / \mu$  is derived using a completely independent method compared to [12, 31].

A more sophisticated analysis, involving fitting Voigt profiles, would not significantly affect our results because the uncertainties in our estimates of the UV redshifts are small compared to the offset between  $z_{21}$  and  $z_{\text{UV}}$ . While more data will improve our estimate of  $\Delta v_{\text{los}}$ , a sample of  $\sim 100$  21-cm/UV absorbers is required before averaged line-of-sight velocity differences and individual redshift measurement errors are similar.

We thank A. Wolfe for data and useful discussions.

\* Electronic address: pana@phys.unsw.edu.au

- [1] J.-P. Uzan, *Rev. Mod. Phys.* **75**, 403 (2003).
- [2] V. A. Dzuba, V. V. Flambaum, and J. K. Webb, *Phys. Rev. Lett.* **82**, 888 (1999).
- [3] J. K. Webb *et al.*, *Phys. Rev. Lett.* **82**, 884 (1999).
- [4] J. K. Webb *et al.*, *Physical Review Letters* **87**, 091301 (2001).
- [5] M. T. Murphy, J. K. Webb, and V. V. Flambaum, *Mon. Not. R. Astron. Soc.* **345**, 609 (2003).
- [6] H. Chand *et al.*, *A&A* **417**, 853 (2004).
- [7] R. Srikanand *et al.*, *Phys. Rev. Lett.* **92**, 121302 (2004).
- [8] R. I. Thompson, *Astrop. Lett.* **16**, 3 (1975).
- [9] C. B. Foltz, F. H. Chaffee, and J. H. Black, *Astrophys. J.* **324**, 267 (1988).
- [10] D. A. Varshalovich and S. A. Levshakov, *J. Exp. Theor. Phys. Lett.* **58**, 237 (1993).
- [11] A. V. Ivanchik *et al.*, *Astronomy Letters* **28**, 423 (2002).
- [12] W. Ubachs and E. Reinhold, *Phys. Rev. Lett.* **92**, 101302 (2004).
- [13] S. Curran *et al.*, *Mon. Not. R. Astron. Soc.* **356**, 1509 (2005).
- [14] A. D. Tubbs and A. M. Wolfe, *Astrophys. J.* **236**, L105 (1980).
- [15] A. M. Wolfe and M. M. Davis, *Astron. J.* **84**, 699 (1979).
- [16] L. L. Cowie and A. Songaila, *Astrophys. J.* **453**, 596 (1995).
- [17] A. M. Wolfe, F. H. Briggs, and D. L. Jauncey, *Astrophys. J.* **248**, 460 (1981).
- [18] P. Tzanavaris *et al.* (2004), astro-ph/0412649, online preprint version of this paper.
- [19] P. Tzanavaris *et al.* (2005), *Mon. Not. R. Astron. Soc.*, in preparation.
- [20] A. M. Wolfe *et al.*, *Astrophys. J.* **294**, L67 (1985).
- [21] N. Kanekar and J. N. Chengalur, *A&A* **369**, 42 (2001).
- [22] N. Kanekar and J. N. Chengalur, *Mon. Not. R. Astron. Soc.* **325**, 631 (2001).
- [23] R. L. Brown and R. E. Spencer, *Astrophys. J.* **230**, L1 (1979).
- [24] A. M. Wolfe *et al.*, *Astrophys. J.* **222**, 752 (1978).
- [25] K. M. Lanzetta and D. V. Bowen, *Astrophys. J.* **391**, 48 (1992).
- [26] A. M. Wolfe, private communication.
- [27] J. X. Prochaska, *Astrophys. J.* **582**, 49 (2003).
- [28] C. L. Carilli *et al.*, *Physical Review Letters* **85**, 5511 (2000).
- [29] A. Songaila *et al.*, *Nature* **371**, 43 (1994).
- [30] V. V. Flambaum *et al.*, *Phys. Rev. D* **69**, 115006 (2004).
- [31] P. Petitjean *et al.*, *Comptes Rendus Acad. Sci. (Paris)* **5**, 411 (2004).
- [32] There are no errors for Q1127–145 (we used the error from [21] as the same instrument was used by the same observers).
- [33] For the single transition in Q0235+164, Q0952+179 and Q0827+243 we used  $6 \times 10^{-6}$ . This is the maximum error of all other  $\langle z_{\text{UV}} \rangle$  except for the atypical value for Q1229–021.
- [34] We adopt  $\Delta x/x = 0$  at  $z = 0$  as the terrestrial value. This has not been checked elsewhere within the Galaxy, and should thus be taken as an assumption.
- [35] For Q0235+164 and Q1127–145 results based on digitized plots have been used in this calculation as there are

no available literature values.

[36] All results here were obtained using method 3.

[37] [31] note that some systematics are probably hidden, in particular in the laboratory wavelengths.

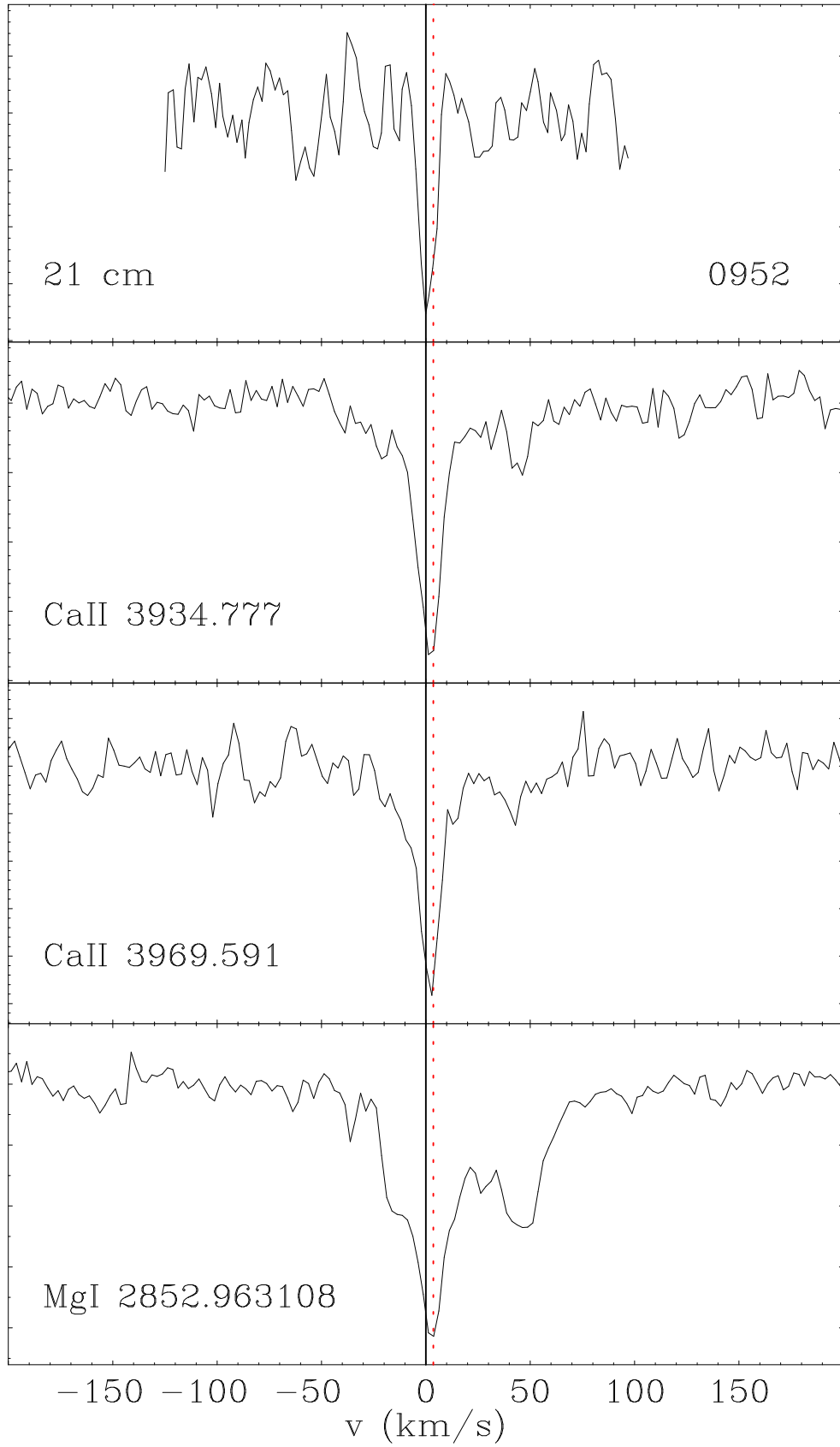


FIG. 2: Velocity plot for 21-cm and UV absorption towards quasar Q0952+179. The solid vertical line at  $0 \text{ km s}^{-1}$  is at  $z_{21}$ . The dotted vertical line is at  $\langle z_{UV} \rangle$ . In this and subsequent plots Ca II is shown for illustration only but has not been used in the calculation of the plotted  $\langle z_{UV} \rangle$ .

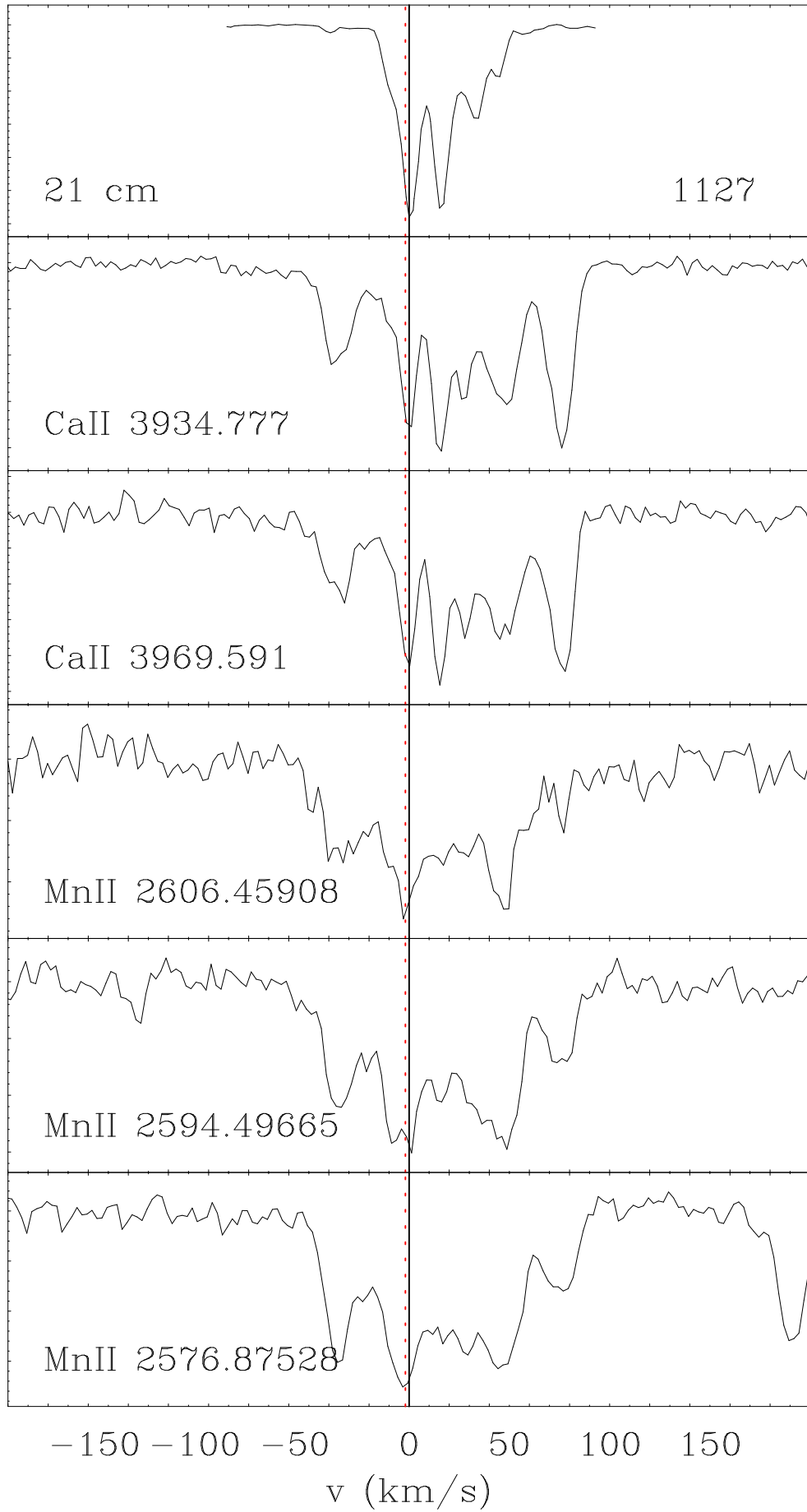


FIG. 3: Velocity plot for 21-cm and UV absorption towards quasar Q1127–145. The solid vertical line at  $0 \text{ km s}^{-1}$  is at  $z_{21}$ . The dotted vertical line is at  $\langle z_{\text{UV}} \rangle$ .

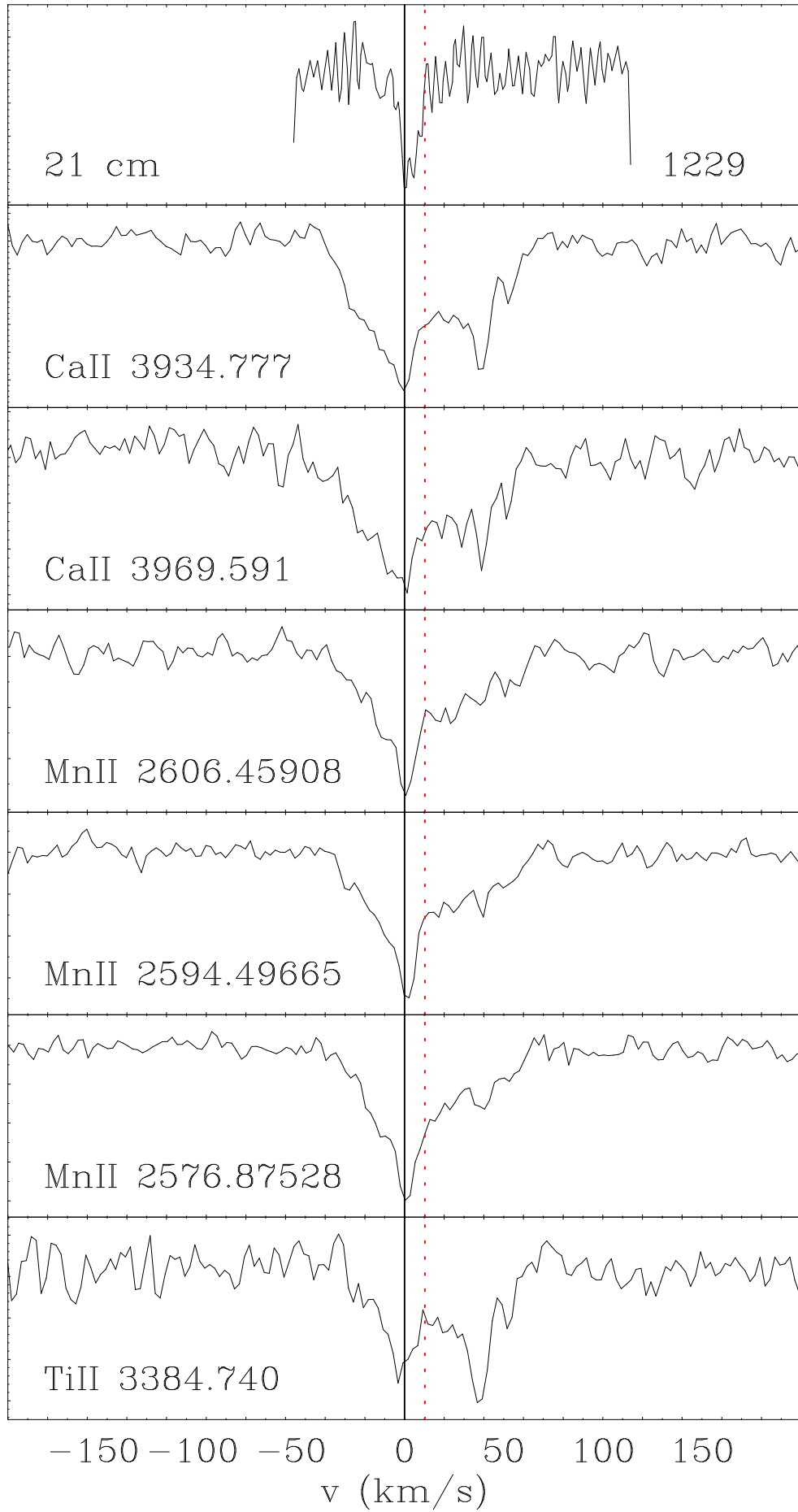


FIG. 4: Velocity plot for 21-cm and UV absorption towards quasar Q1229-021. The solid vertical line at  $0 \text{ km s}^{-1}$  is at  $z_{21}$ . The dotted vertical line is at  $\langle z_{UV} \rangle$ .

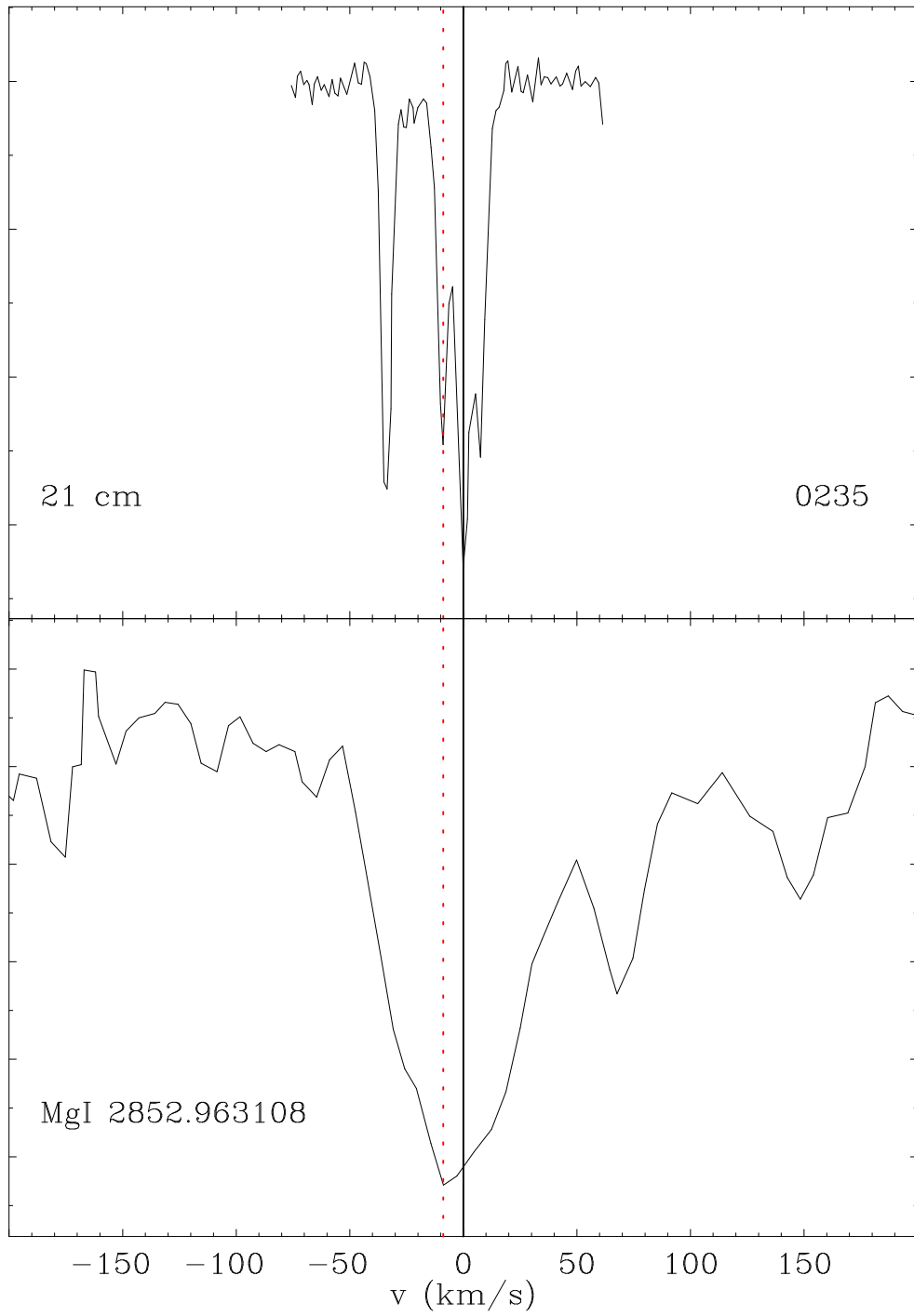


FIG. 5: Velocity plot for 21-cm and UV absorption towards quasar Q0235+164. The solid vertical line at  $0 \text{ km s}^{-1}$  is at  $z_{21}$ . The dotted vertical line is at  $\langle z_{UV} \rangle$ .

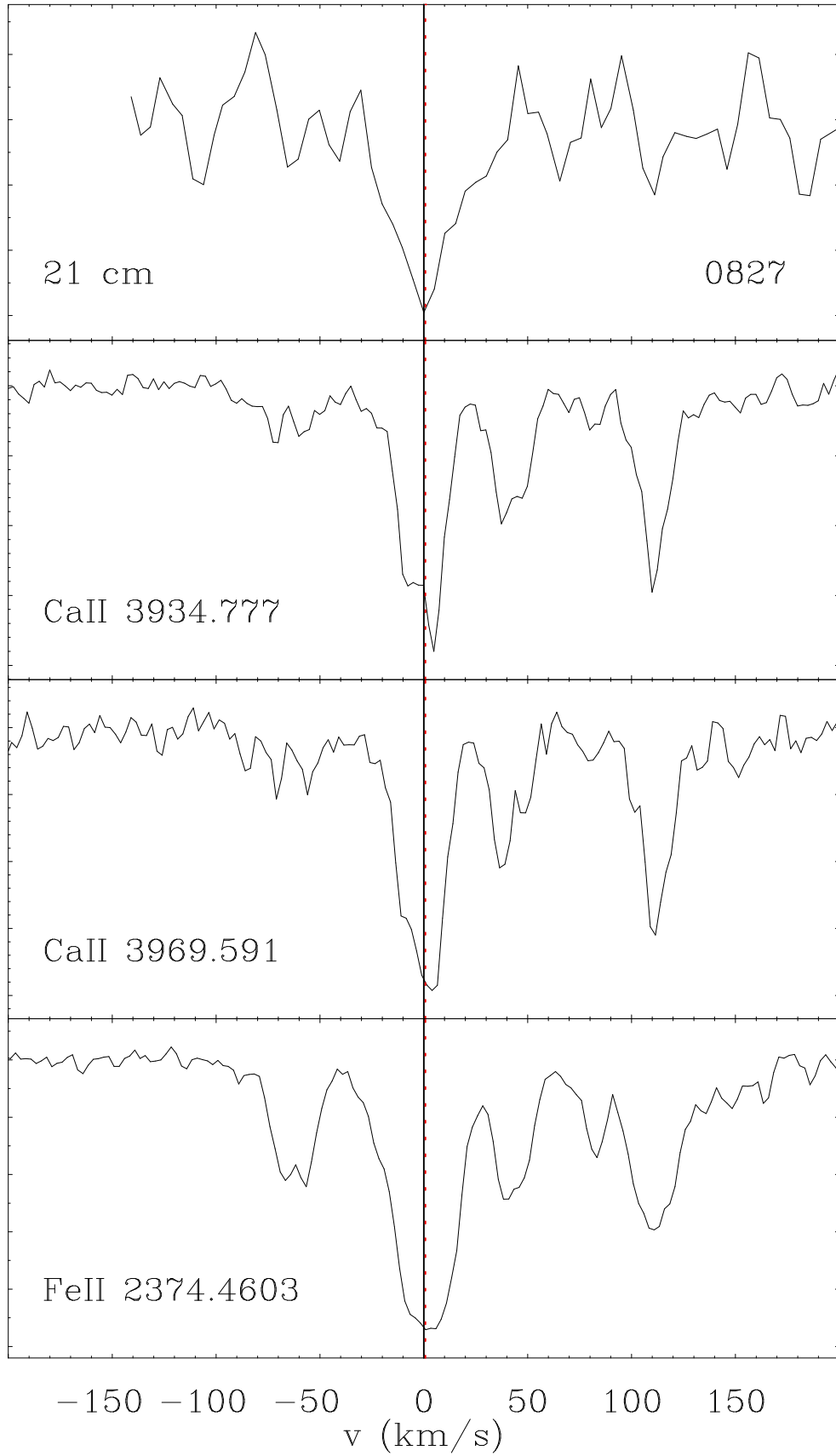


FIG. 6: Velocity plot for 21-cm and UV absorption towards quasar Q0827+243. The solid vertical line at  $0 \text{ km s}^{-1}$  is at  $z_{21}$ . The dotted vertical line is at  $\langle z_{\text{UV}} \rangle$ .

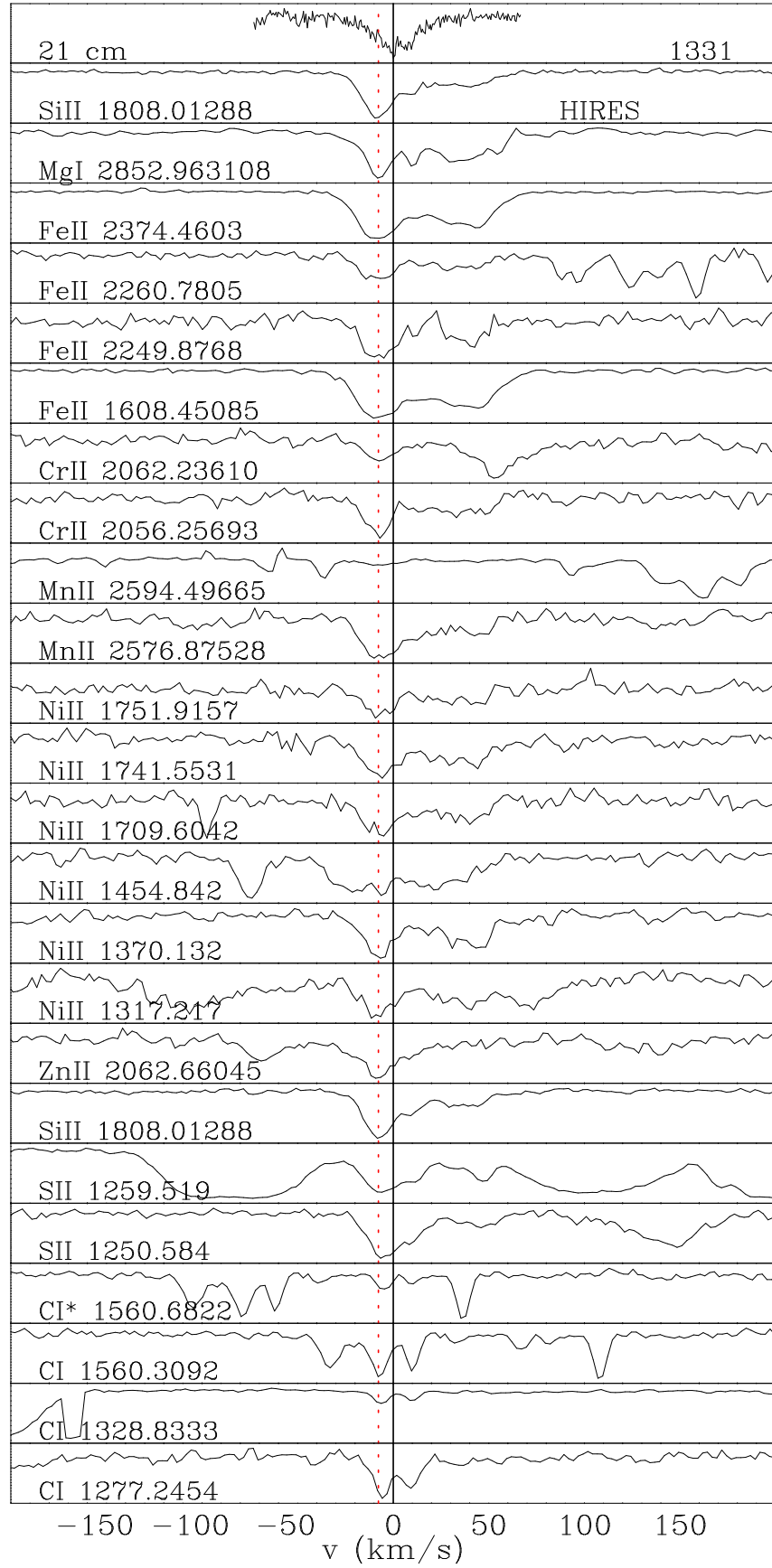


FIG. 7: Velocity plot for 21-cm and UV absorption towards quasar Q1331+170. The solid vertical line at  $0 \text{ km s}^{-1}$  is at  $z_{21}$ . The dotted vertical line is at  $\langle z_{UV} \rangle$ .

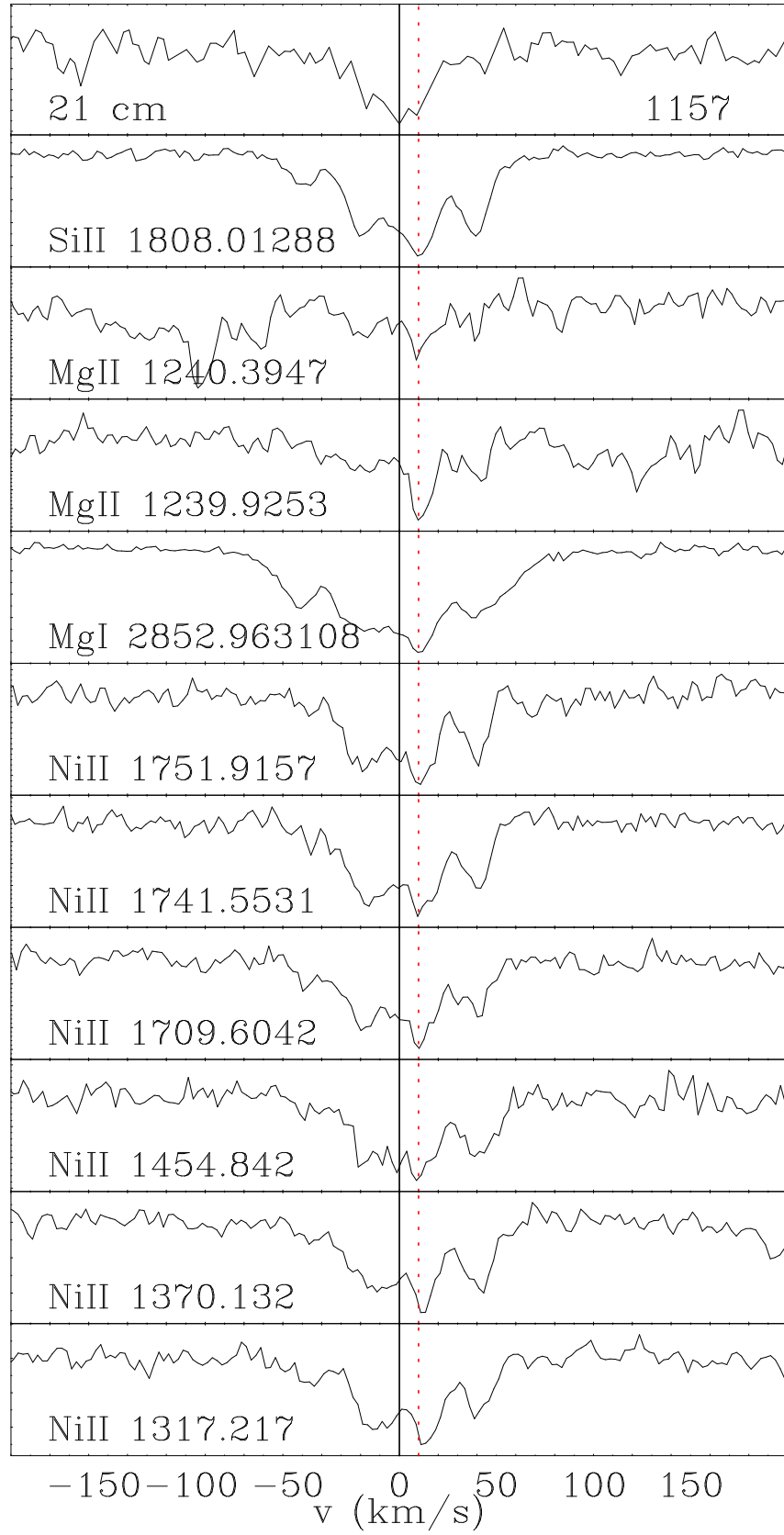


FIG. 8: Velocity plot for 21-cm and UV absorption towards quasar Q1157+014. The solid vertical line at  $0 \text{ km s}^{-1}$  is at  $z_{21}$ . The dotted vertical line is at  $\langle z_{UV} \rangle$ .

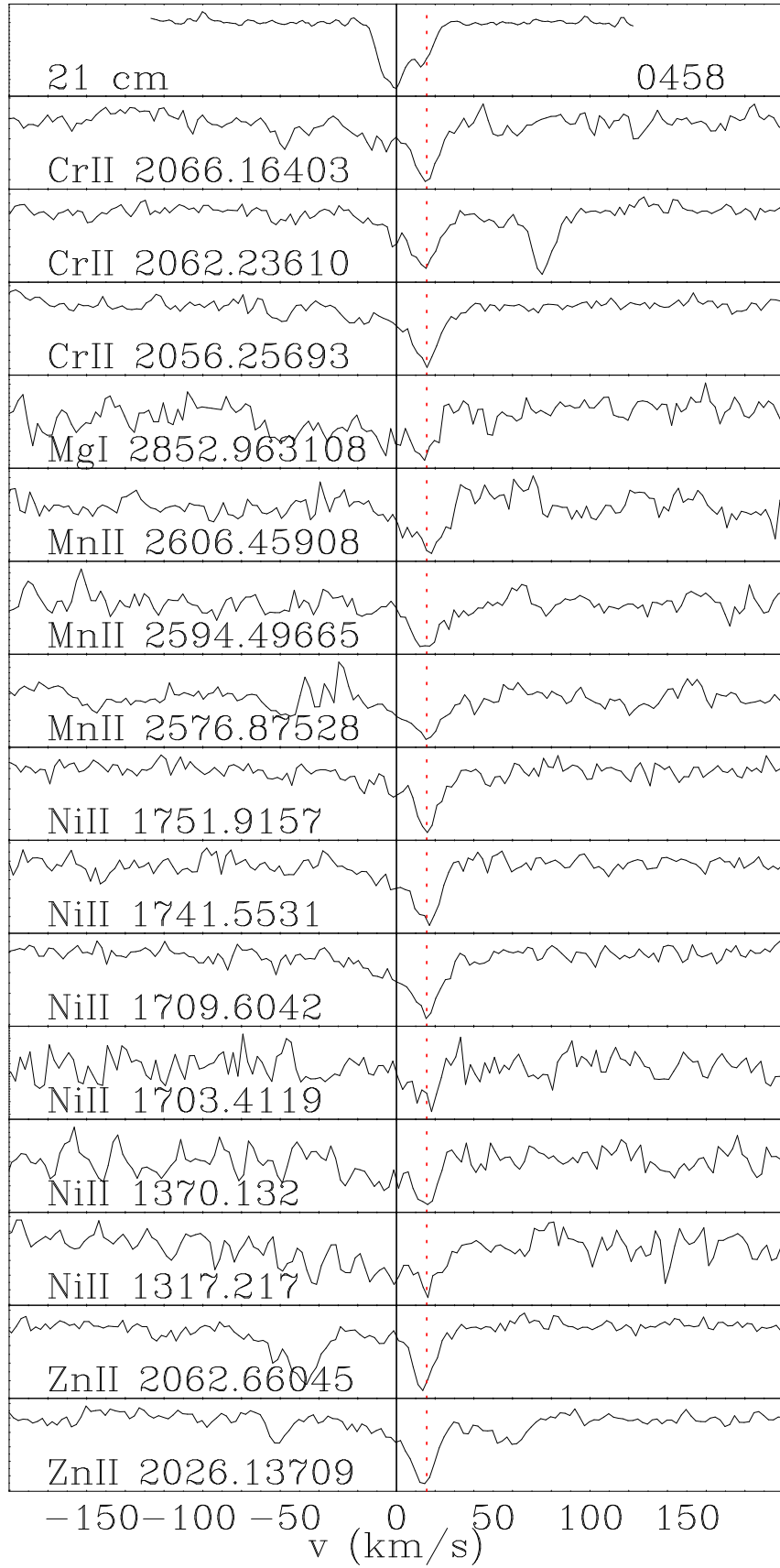


FIG. 9: Velocity plot for 21-cm and UV absorption towards quasar Q0458-0203. The solid vertical line at  $0 \text{ km s}^{-1}$  is at  $z_{21}$ . The dotted vertical line is at  $\langle z_{UV} \rangle$ .